Mechanisms of flame propagation in jet fuel sprays as revealed by OH/fuel planar laser-induced fluorescence and OH* chemiluminescence

Pedro M. de Oliveira, Epaminondas Mastorakos

Hopkinson Laboratory, Department of Engineering, University of Cambridge, Cambridge, CB2 1PZ, UK

Abstract

Previous work on spray flames has shown that different propagation mechanisms may occur depending on the size and number density of droplets. In this work, the structure and propagation of flames in uniformly dispersed sprays of low-volatility fuels is experimentally examined. The effect of the Sauter mean diameter (SMD) of the spray (16-33 µm) on the propagation modes, flame speed, and flame curvature is assessed in weakly turbulent sprays, with the ratio of axial velocity rms to the gaseous laminar burning velocity $u'_z/S_{L,g}$ ranging from 0.5-2.5, and overall equivalence ratio ϕ of 0.8, 1, and 1.4. The growth of the flame is evaluated from OH*-chemiluminescence and schlieren visualisation, which combined to OH/fuel planar laser-induced fluorescence visualisation reveal details of the propagation mechanisms. The aviation fuels investigated – Jet A and a renewable alternative, ATJ-8 – exhibited similar flame speed behaviour due to changes in SMD in each of the propagation modes identified: the droplet, inter-droplet, and gaseous-like modes. Concentrated reactions around large droplets found in lean conditions (ϕ= 0.8) allowed for a slowly propagating flame front which, in turn, ignited new droplets. Stoichiometric to rich conditions (ϕ=1, 1.4) were marked by stronger evaporation ahead of the flame and, therefore, higher and more uniform heat release across the flame. Still, droplets penetrated the flame, locally inducing regions of negative flame curvature and continuing to evaporate in the burnt products. The droplet-induced effects disappeared at low SMD (16 µm, ϕ=1.4), giving rise to a fully gaseous layer ahead of the flame

Email address: pm580@cam.ac.uk (Pedro M. de Oliveira)

and the highest flame speeds. At rich conditions and high SMD, Jet A had a lower flame speed than ATJ-8.

Keywords:
spray combustion, flame propagation, jet fuels

1. Introduction

The development of cleaner and more efficient aviation engines operating with non-petroleum fuels relies on fundamental understanding of the processes controlling the operating envelope of the engine: the ignition and lean blow-off of the flame. In the present work, the droplet-flame interactions and their role in the propagation mechanisms of the flame are investigated, thus addressing a common feature of both transient processes found in gas turbine combustors.

Some of the fundamental ideas concerning flame propagation in sprays were first introduced in the early experimental work of Burgoyne and Cohen [1], who verified that the size of the droplets played an important role in determining the propagation characteristics of a tetralin-air flame. A propagation behaviour similar to a gaseous flame was observed in experiments with small droplet sizes, while a transition to propagation through individually burning droplets occurred as the droplets became larger, increasing from $10\,\mu$m to $55\,\mu$m. Following this work, a number of other experiments [2–12] mainly observed a detrimental effect of increasing the droplet size of the spray on flame speed, which was verified through parametric studies considering the spray, mixture, and flow characteristics. This was attributed to the fact that part of the energy released by the flame is required to vaporise the fuel droplets, which is usually controlled by long evaporation timescales [13]. Hence, decreasing the amount of prevaporised fuel or varying any parameters of the two-phase mixture in order to reduce evaporation rates can be expected to have a detrimental impact on flame speed. However, it has been shown in [1, 5–7, 10, 11] that the flame speed in a spray can be enhanced at optimal droplet sizes, that is, it can be higher than the laminar burning velocity of a gaseous mixture with the same equivalence ratio.

To account for this effect, the propagation of the flame across a droplet mist has been modelled as a combination of individually burning droplets and homogenous reaction in a gaseous mixture [14], improving the previous model proposed in [8]. In fact, this mechanism comprising a homogenous

reaction occurring in rapidly evaporating droplets and an additional relay-transfer propagation between large droplets has been first proposed in [2] and further developed in [15], simply based on limited macro-scale photographs of the flames. This approach has led to an improved prediction of the unusually high values of flame speed found in experiments.

The contrasting results of experiments and lack of detailed information on the flame structure due to the complexities involved in spray experiments motivated recent work on this topic using direct numerical simulations (DNS). In DNS of igniting spherically expanding flames in sprays, the droplet-scale structure of the flame and its development have been observed with simplified [16–19] and complex chemistry [20]. In the work of Neophytou et al. [20], two flame propagation mechanisms according to the early description of [2] were identified, namely the droplet and the inter-droplet ignition modes, which were observed up to 1.5 times the chemical timescale of the flame after the spark, that is, similar to the critical time scale verified in experiments [21]. The droplet ignition mode was observed in dilute sprays with Group number [22] $G < 6$ and exhibited propagation through bridges of mixture fraction in a below-flammable inter-droplet space, driven by diffusion of heat and species from individually burning droplets. A different mechanism was verified in dense sprays (G=20), where a more homogenous flame front was found due to strong droplet evaporation occurring in the pre-heat layer of the flame and reaction occurring in near-stoichiometric mixture fraction conditions.

Flame propagation is a key factor controlling the early-phase ignition of sprays; a process that comprises the generation of a *flame kernel* [23], and can be understood based on a critical time scale concerning the duration of the spark effects on the flame [21]. First, a flame kernel is formed by external deposition of energy generating a high-temperature plasma, which subsequently cools to near-adiabatic flame temperatures [16]. Insight can be drawn from autoignition processes [24] to understand this spark-controlled phase, as failure to establish a kernel is usually attributed to factors leading to a slow autoignition process [23]. Following the cooling of the plasma, a net increase of chain-branching reactions occurs [25, 26], marking the end of the overdriving effects of the spark. At this point, successful ignition of the kernel depends solely on the propagation of the flame into the fresh mixture, given fuel is readily available and that heat losses to the surrounding flow are overcome [23]. The presence of fuel droplets in the flow and their interaction with the flame, turbulence, as well as with each other, increases the complexity of this propagation-controlled phase and, therefore, must be

considered.

Moreover, important droplet-scale phenomena have been identified as main factors controlling flame propagation, such as the presence of mixture inhomogeneities as well as droplet-induced increase of flame surface area due to wrinkling [4, 7, 11, 27]. The effective equivalence ratio was defined as the actual equivalence ratio at the inter-droplet spacing resulting from fuel evaporation between the fresh mixture and the high-temperature region ahead of the flame [7]. The importance of this parameter was verified in DNS [17, 20, 28, 29], in which preferential flame propagation was observed in regions of optimal equivalence ratio near stoichiometry. Additionally, the contribution of droplet-induced curvature in DNS of laminar and turbulent spray flames has also been verified to increase with droplet size of the spray [18, 19]. Further, droplet penetration through the flame leading to additional fuel influx reaching the flame front from the burnt products side [16, 28] and possibly undergoing pyrolysis in that region due to high temperatures [20] have also been observed to give rise to high flame speeds in sprays in addition to droplet-induced wrinkling and mixture inhomogeneities. Some evidence of droplet penetration has been verified in spherically expanding flame experiments directly through schlieren [30] and by tracking the sudden change of velocity of ethanol droplets as they crossed the flame [27]. At those conditions, triggering of Darrieus-Landau instabilities leading to flame wrinkling was observed through schlieren and associated with the phenomenon of droplet penetration across the reaction zone [27]. This phenomenon has been demonstrated to be an important feature of stable spray flames [1]. As visualised in a spray jet flame [31], large droplets with high momentum transport significant amounts of fuel to secondary regions of the flame, as they survive the flame's leading edge near the injection nozzle. The presence of several large droplets at the reaction zone may locally induce high fluctuations of heat release and even promote local extinction by intense evaporative cooling [31, 32].

Thus far, there has been no experimental droplet-scale visualisation of the interaction between the droplets and the flame nor experimental evidence of the propagation mechanisms in turbulent spray flames and the range of conditions in which they occur. Typically, DNS has been used to investigate these aspects of spray flames, but this approach is limited due its modelling assumptions of the spray and the combustion chemistry, often not meeting certain conditions relevant to real applications. Advanced diagnostics provide an opportunity of measurements to be taken at droplet scale in

canonical experiments while featuring polydiserse sprays and complex multi-component fuels – two aspects especially relevant to gas turbine combustion. In this work, the problem of a spherically expanding flame is investigated in a uniformly distributed droplet field advected by a weakly-turbulent flow with constant mean velocity, which preliminary results have been presented in [33, 34]. The main objectives of this study are:

1. Visualise the structure of spray flames and their propagation modes at the droplet scale using OH*-chemiluminescence, schlieren, and simultaneous OH/fuel planar laser induced fluorescence (PLIF), quantifying the impact of the droplets on the flame structure through an evaluation of the two-dimensional flame curvature.
2. Experimentally evaluate the turbulent flame speed of two jet fuels, Jet A and ATJ-8 (a renewable alcohol-to-jet fuel) as a function of the spray's SMD and overall equivalence ratio by using OH*-chemiluminescence visualisation. Both fuels are real aviation fuels, with each specific fuel batch being well characterised in terms of thermophysical and chemical properties [35, 36] as well as laminar burning velocities [37], mainly differing in composition and in terms of distillation characteristics.

2. Methods

2.1. Experimental work

2.1.1. Burner

The experimental apparatus used in the present work has been previously presented in detail [21], thus, only its main characteristics are described in this section for completeness. The apparatus shown in Fig. 1 consists of a burner, i.e. a diverging-converging tube, where the liquid fuel is atomised by an air-assist atomiser and carried by the main air flow. The two-phase flow passes through a converging section and exits the burner through a 20.8-mm diameter nozzle, forming a jet characterised by a top-hat velocity profile, uniform turbulence, and uniform distribution of droplet sizes across its diameter, as discussed in [21]. The droplet size distribution is set between a fine monodisperse-like spray and a coarse spray by adjusting the air flow rate into the atomiser while keeping constant the total air flow and the fuel flow. Thus, the droplet size is adjusted independently of the overall equivalence

Table 1: Thermochemical surrogate composition of the aviation fuels studied [35].

Name	*Surrogate composition*	*Avg. form.*
Jet A	15% 1,2,4-trimethylbenzene (C_9H_{12}) 30% iso-dodecane ($iC_{12}H_{26}$) 20% n-undecane ($nC_{11}H_{24}$) 35% pentyl-cyclohexane ($MC_{11}H_{22}$)	$C_{11}H_{22.1}$
ATJ-8	85% iso-dodecane ($iC_{12}H_{26}$) 15% iso-hexadecane ($iC_{16}H_{34}$)	$C_{12.6}H_{27.2}$

ratio of the mixture. A detailed characterisation of the spray is presented in Sec. 3.1, showing that the resulting Sauter mean diameter (SMD) was between 16 and 33 µm. The preheating temperature of the air is set to 100 °C, resulting in partial prevaporisation of the fuel droplets inside the burner. An equivalence ratio of the gas phase, ϕ_g, of approximately 0.3 was estimated using the First-Law energy balance approach given in [21], but taking into account the temperature of the mixture at the outlet of the burner.

The jet exiting the nozzle is characterised by a polydisperse spray uniformly distributed in a mixture of fuel vapour and air. In the centre of the jet, a flame is initiated by focusing a 532-nm Nd-YAG laser at 5 mm downstream of the nozzle. The ignition energy of the laser is set between 10 and 50 mJ by adjusting the Q-switch delay of the laser and measuring each pulse with pyroelectric energy sensors. Given breakdown of the mixture is promoted by the laser spark initiating a small flame kernel, the kernel may grow or quench while it is convected by the bulk flow. Issues concerning the stochastic behaviour of the ignition process were the focus of previous experiments with ethanol sprays [21]. In this work, experiments are carried out with jet fuel and attention is given only to spark events resulting in the development of a self-sustained flame, which is observed in the absence of large-scale inhomogeneities and free from mixing effects.

2.1.2. Fuels

To study the effect of droplet size on the flame propagation characteristics in sprays of low-volatility multi-component fuels, two jet fuels were selected. The standard Jet A was compared to the ATJ-8, a commercial renewable jet fuel derived from isobutanol through the alcohol-to-jet process. Both ATJ-8 and Jet A fuels are being studied under the United States' *National Jet Fuel Combustion Program* [36], being referred to as C-1 and A-2, respectively,

following the nomenclature of the program. The fuels' thermochemical surrogate composition is shown in Table 1 for reference. ATJ-8 (C-1) is a fuel formed primarily of C_{12} and C_{16} iso-paraffins, with 1% of aromatic content [35], hence resulting in a characteristic bimodal distillation curve shown in Fig. 2a. Additionally, Jet A and ATJ-8 present similar thermophysical properties controlling evaporation, that is, vapour pressure, specific heat, as well as enthalpy of vaporisation of approximately 300 kJ/kg [35] (Fig. 2). Thus, the resulting molar fraction of fuel in the gas phase is expected to be similar between experiments with the two fuels, although a minor variation of ϕ_g should occur due to the difference in the fuels' average molecular formulas. Additionally, both fuels present similar laminar burning velocities, with Jet A presenting approximately 10% higher S_u° than ATJ-8 [37].

2.1.3. Visualisation and flow velocity

The flame is visualised in two different sets of experiments, shown in Fig. 3. Simultaneous high-speed OH*-chemiluminescence and schilieren visualisation is carried out for a wide range of flow conditions, from which the flame speed is evaluated. Additionally, simultaneous OH and fuel planar laser-induced fluorescence provides a more detailed visualisation of the flame front and the spray in the cross-sectional plane formed by the ignition beam and the axis of the jet. In both experiments, the visualisation of the flame is carried out within the first jet diameter downstream of the nozzle. A region of 20×20 mm immediately downstream of the nozzle is imaged, characterised by uniform velocity and droplet size profiles and also free from entrainment of ambient air [21].

In the PLIF experiments (Fig. 3a), a single 283-nm laser sheet is used to excite the fuel and the $Q_1(6)$ transition in the (1,0) vibrational band of the OH. The fluorescence signal of the fuel and of the OH are individually collected by two high-speed CMOS cameras (Photron SA1.1) coupled with a two-stage image intensifier (LaVision HS-IRO, 500-ns gate), a Scheimpflug extension bellow, and identical 100-mm UV lens. In the first camera, a narrow band filter (10-nm FWHM) centred at 310 nm is used for the OH fluorescence, thus blocking most of the wide-band fuel fluorescence as well as the Mie scattering from the droplets. In the second camera, the fuel fluorescence is captured using a 310-nm long pass filter, which blocks the Mie scattering and the OH fluorescence. The fluorescence of the kerosene is attributed to the fuel's aromatic content, and occurs mostly between the wavelengths of 320 nm and 360 nm once excited at approximately 283 nm, as

experimentally demonstrated by Orain et al. [38].

The 283-nm beam is obtained from a high-repetition diode-pumped solid-state laser (JDSU Q201-HD, 532 nm, 14 W at 5 kHz, 18-ns pulse length) which pumps a high-speed dye laser (SIRAH Credo model 2400) with a solution of rhodamine 6G and ethanol. The resulting 566-nm beam is doubled by a BBO crystal and tuned at approximately 283 nm (at 300 mW, 60 μJ/pulse). Sheet-forming optics are used (Fig. 3a, 1-3) to produce a sheet of 20 mm in height and approximately 0.1 mm in thickness, that is, of the same order of the largest droplets. The sheet passes through a cut-off plate, which blocks most of the diverging 532-nm ignition beam coming from the opposite direction and aligned with the 283-nm sheet. The fluorescence signals of both cameras are post-processed to correct for the sheet's energy profile and pulse-to-pulse fluctuations.

In the line-of-sight experiments (Fig. 3b), the high-speed cameras are operated at 12 kHz and 80-μs exposure time. The camera setup used for OH* chemiluminescence is the same as in the PLIF experiments, except for the use of a wider (25-nm FWHM) 310-nm band-pass filter. All imaging parameters of the system (e.g., gain, aperture, and shutter speed) were kept the same during the experiments so that the OH* signal, representing the approximate heat release in the flame [39], could be directly compared between conditions. The schlieren system comprised of a CMOS camera (non-intensified), two plano-convex lenses (200-mm and 500-mm), a 1-mm optical fibre and a Xenon light source (Karl-Storz Xenon Nova 300). A 1.5-mm cut-off iris is also used with a long-pass 475-nm filter to improve the sharpness of the image. A resulting nominal resolution of 31.2 μm/pixel is achieved in the line-of-sight visualisation, while 15.6 μm/pixel is achieved in PLIF imaging.

Prior to the visualisation experiments, a number of non-reacting tests were carried out to identify the operating conditions at which a spray flow with SMD of 16, 22, 28, and 33 μm could be obtained for overall equivalence ratios of 0.8, 1, and 1.4. For that, flow velocity and droplet size measurements were performed with a Dantec FiberFlow while recursively adjusting the carrier and the atomising air flow rates until the desired condition was achieved. The system consisted of an Argon-Ion laser, a 500-mm transmitting probe, and a 310-mm receiving probe. The probes were positioned at an angle of 30° off-axis from the forward scattering direction, allowing for axial velocity measurements and droplet size measurements up to 80 μm, approximately. Measurements were taken at the centre of the jet, at the exit of the burner. For each measurement, approximately 20000 samples were obtained

Table 2: Summary of experimental conditions

Experimental conditions	
Fuels	Jet A, ATJ-8
Sauter mean diameter	16, 22, 28, 33 µm ± 1 µm
Equivalence ratio	0.8, 1, 1.4
Preheat air temperature	100 °C
Outlet temperature	82 °C ± 2 °C
Bulk flow velocity	7.7 m/s ± 0.3 m/s
Axial velocity rms	0.2–0.6 m/s
Incident laser energy	10, 20, 50 mJ

at 1-kHz data rate and above 95% validation rates.

The experiments were performed for the conditions mentioned previously, summarised in Table 2. For mixtures with an overall equivalence ratio ϕ_o of 0.8, 1, and 1.4, the incident laser energy was set as 50, 20, and 10 mJ, respectively, resulting in roughly 50% of probability of a flame kernel to ignite. At each test condition, 360 ignition attempts were performed at 2 Hz in the line-of-sight experiments and 1 Hz in the PLIF experiments. Additionally, a photodiode was used to monitor each spark event, independently triggering the cameras after 150 µs.

2.2. Flame speed

2.2.1. Measurement technique

Each OH* image sequence corresponding to an ignition event was binarised based on an absolute threshold. The projected area of the flame A_f was evaluated from the binarised images, from which the mean radius of the flame $r_f(t)$ was obtained by assuming an spherical flame, that is, $r_f = \sqrt{A_f/\pi}$. The burnt flame speed S_b was evaluated as,

$$S_b = \frac{dr_f}{dt}. \tag{1}$$

Further, the unburned flame speed was estimated [40],

$$S_u = S_b \frac{\rho_b}{\rho_u}, \tag{2}$$

where ρ_b and ρ_u are the the densities of the burned and unburned gases, respectively. Here, a series of approximations were made to estimate ρ_b and

ρ_u, since the local (effective) equivalence ratio at which the flame burns is unknown as liquid droplets may survive the flame, being found in the burnt products. In the present approach to estimate S_u, the unburnt density was evaluated based on the density of the reactants assuming full vaporisation of the fuel at the overall equivalence ratio and temperature equal to the measured temperature at the outlet of the nozzle. Additionally, the burnt density was evaluated at the adiabatic flame temperature for that mixture.

The unburnt flame speed was evaluated in respect to time for each individual ignition event. Thus, a mean value $\overline{S}_u$ corresponding to the unburnt flame speed of a self-sustained flame at a given flow condition was calculated considering ignition events only. For that, a time-averaged value of S_u for each ignition event was used, based on the last four images of the sequence, before the flame reached any of the limits of visualisation window. At this point, the effects of the spark on the flame were observed to be negligible, as discussed in [21]. Still, due to the relatively small size of the flame kernels limited by the jet diameter as well as the visualisation window, some effect of stretch due to the mean curvature of the flame can still be expected.

Additionally, the flame curvature was evaluated from the OH PLIF image sequence. The burnt and unburnt regions were defined based on an absolute threshold corresponding to a progress variable of approximately 0.5. From that, the flame front was described as a parametric curve $x(s)$ and $y(s)$, and high-frequency variations were filtered using a Fourier-transform low-pass filter. Thus, the local curvature at any point $\mathrm{M}(x, y)$ can be calculated as,

$$\kappa = \frac{x'y'' - y'x''}{(x'^2 + y'2)^{3/2}}, \tag{3}$$

where positive values of κ correspond to a convex flame front in relation to its propagation direction.

2.2.2. One-dimensional calculations

The laminar burning velocity of a gaseous flame, $S^{\circ}_{L,g}$, was obtained from one-dimensional calculations of planar and freely propagating premixed flames. Additionally, these calculations were also used to evaluate ρ_b and ρ_u so that S_u could be estimated. The 1-D calculations were carried out in the software Cosilab [41], using the Dagaut [42] and the GRI-Mech [43] chemical mechanisms for kerosene and methane, respectively. The laminar burning velocity was evaluated for a range of equivalence ratios, and used for comparison with the present experimental data concerning the stretched unburnt

flame speeds in the methane-air spherically-expanding flames (used for validation) and the jet fuel-air spray flames.

2.3. Validation

The proposed method for evaluating the unburnt flame speed was validated through experiments with laminar methane-air flames. For these experiments, the flow lines to the atomiser were kept closed and the total premixed methane-air flow was injected at the bottom of the burner, hence minimising turbulence and improving mixing. Measurements of S_u in methane-air mixtures were carried out in a 3-m/s jet at ambient temperature, with the mixture equivalence ratio varying between 0.7-1.3 and incident laser energies of 40 and 60 mJ. Toroidal-like flame kernels typical of laser ignition were observed for all experimental conditions, developing steadily within the visualisation window as shown in Figs. 4a-b. The instantaneous OH* and schlieren images of the flame moments before reaching the limits of the visualisation window are also shown in (b) and (c), respectively.

The mean stretched unburnt flame speed $\overline{S}_\mathrm{u}$ was evaluated and compared to the unstretched values obtained from Cosilab calculations using the GRI-Mech [43] and the experimental data from [44] (Fig. 5). Consistent results were found between the results for two different energy levels, indicating the suppression of plasma-cooling effects on the flame. Good agreement between the measurements and the numerical and experimental data used as reference was found for lean to stoichiometric mixtures, although some difference between the experimental and reference values was observed for rich mixtures. The latter effect could be associated with stretch effects caused by flame curvature and higher Lewis number found in rich conditions [45]. It is expected that such errors associated with the mean radius of the flame should be of less importance in a spray flame, as droplet-induced curvature and other effects highlighted in Sec. 3 are likely to have a stronger impact on flame speed. Indeed, since the spray flames are wrinkled due to turbulence and due to droplet-scale effects, it is not clear how one could employ, in this case, stretch corrections used to obtain the laminar burning velocity, S_L°, from measurements of stretched laminar flame speed, S_L [40].

3. Results and discussion

3.1. Spray characteristics

The distribution of droplet sizes was controlled by varying the air flow rate into the atomiser, allowing for experiments where d_{32} and ϕ were independently set. The droplet size distributions followed a modified Rosin-Rammler distribution [46],

$$Q(d) = 1 - \exp\left(\frac{\ln(d)}{\ln(X_{\mathrm{m}})}^{q_{\mathrm{m}}}\right) \tag{4}$$

where the parameters X_{m} and q_{m} were obtained by fitting of the experimental data. Rosin-Rammler distributions are shown in Fig. 6 for a lean mixture of ATJ-8 concerning the (a) accumulated liquid volume and (b) probability density functions of droplet size. In the figure and throughout this paper, the colours depict four different degrees of atomisation. Tables 3-4 give the parameters for a modified and regular Rosin-Rammler distributions, respectively, for all spray conditions investigated. Thus, the spray characteristics can be accurately implemented in any future numerical simulations of the present experiment. Further, the Stokes number of the droplets was evaluated based on the longitudinal integral length scale of the flow, L_{11}, and the axial velocity root mean square (rms) fluctuation, u'_z. The integral length scale was evaluated from the normalised autocorrelation of the turbulent fluctuation signal from PDA/LDA measurements, being approximately 9.5 mm [21]. Droplets between 10-30 μm had a Stokes number between 0.01-0.1, thus closely following the flow.

The uncertainty associated with the variation of d_{32} between experiments with a fixed ϕ was approximately $\pm 1\,\mu$m for a confidence interval of 95%, while the derived experimental uncertainty [47] of ϕ was $\pm 0.3\%$. In addition to that, some variation of the axial velocity rms u'_z occurred within the experiments. A negative correlation between u'_z and d_{32} was observed (Fig. 7), as varying the atomising air flow to control atomisation affected the generation of turbulence in the jet through the shear between the spray cone and the carrier flow within the burner. Still, experiments were carried at relatively low turbulence levels corresponding to a regime of weakly corrugated premixed flame ($u'_z/S_{\mathrm{L,g},\phi=1}$ between 0.6-1.4).

Further, the Group combustion number G, representing the ratio of the rate of droplet evaporation to the transport of gaseous species by diffusion

Table 3: Parameters of the Modified Rosin-Rammler distributions.

	Jet A			ATJ-8		
ϕ	d_{32}	X_{m}	q_{m}	d_{32}	X_{m}	q_{m}
0.8	33	50.1	8.38	33	47.8	8.66
0.8	27	44.7	7.23	28	40.0	7.35
0.8	23	38.0	6.12	23	34.6	6.62
0.8	16	27.9	5.04	16	25.7	5.29
1.0	32	52.9	8.87	34	47.3	7.72
1.0	28	46.4	7.59	29	42.6	7.35
1.0	21	38.5	6.13	23	32.7	5.85
1.0	17	28.0	5.01	16	26.1	5.29
1.4	33	52.3	8.64	33	48.6	7.75
1.4	27	47.0	7.36	28	42.9	6.71
1.4	21	37.4	6.34	23	31.8	6.43
1.4	16	28.2	5.20	17	21.9	5.75

Table 4: Parameters of the Rosin-Rammler distributions.

	Jet A			ATJ-8		
ϕ	d_{32}	X	q	d_{32}	X	q
0.8	33	48.5	2.30	33	50.8	2.20
0.8	27	40.7	2.05	28	45.6	1.95
0.8	23	35.3	1.92	23	39.0	1.72
0.8	16	26.4	1.68	16	28.9	1.54
1.0	32	48.2	2.06	34	53.6	2.30
1.0	28	43.4	2.01	29	47.2	2.03
1.0	21	33.5	1.72	23	39.5	1.71
1.0	17	26.9	1.68	16	28.9	1.53
1.4	33	49.4	2.06	33	53.2	2.24
1.4	27	43.8	1.83	28	47.8	1.96
1.4	21	32.4	1.93	23	38.3	1.79
1.4	16	22.3	1.98	17	29.1	1.59

[22], given as,

$$G = 3\left(1 + 0.276 * \mathrm{Re}_{\mathrm{d}}^{1/2}\mathrm{Sc}^{1/3}\right)\mathrm{Le}N^{2/3}\left(d/l_{\mathrm{d}}\right) \tag{5}$$

where Re_{d} is the droplet Reynolds number, and Sc and Le are the Schmidt

number and the Lewis number of the kerosene vapour-air mixture, respectively. The parameter d is the droplet diameter, evaluated as simply the Sauter mean diameter of the flow, d_{32}. In order to evaluate the the number of droplets in the cloud N and the mean droplet spacing l_{d}, a volume with characteristic length of the order of L_{11} was assumed. Within the present conditions, G increased with ϕ and d_{32}, ranging from approximately 10 to less than 100 for ϕ of 0.8 and 1, and to over 100 for ϕ of 1.4. The range of $1 < G < 100$ represents the external combustion mode [22], and is characterised by an increasing droplet burning rate from the centre of the cloud towards its outer layer as as G increases. For higher values of G, above 100, the combustion mode was defined as sheath combustion, which indicates that droplet vaporisation within the cloud is negligible and occurs mostly in a thin external layer of the cloud [22]. In Sec. 3.3, G and ϕ are used to classify the experimental conditions in terms of the propagation modes observed.

3.2. Flame speed and general characteristics

The effect of the spray SMD on the unburnt flame speed of Jet A and ATJ-8 is shown in Fig. 8a. The measurements were also given in terms of the overall equivalence ratio of the mixture for comparison with the calculated gaseous premixed laminar burning velocity (b). Overall, increasing the polydispersity of the spray and consequently its SMD was detrimental to $\overline{S}_{\mathrm{u}}$ (Fig. 8a). This effect was verified in stoichiometric and rich mixtures of both fuels, with ATJ-8 being faster than Jet A as the SMD increased in rich conditions. Also, the measured flame speeds were generally lower than the gaseous laminar burning velocity for a mixture with the same ϕ (Fig. 8b). This distinct difference between $S_{\mathrm{u}}(\phi)$ of the spray and $S^{\circ}_{\mathrm{L,g}}(\phi)$ indicates that one of the controlling parameters of flame speed in spray flames is the effective equivalence ratio at the leading edge of the propagating front rather than the overall equivalence ratio of the spray, ϕ, as pointed out in previous numerical works [17]. Thus, spray flames usually propagate at a leaner equivalence ratio than the overall equivalence ratio of the mixture [28, 19] and may present S_{u} values that are significantly higher than the stoichiometric gaseous condition, as in cases with ϕ =1.4 for all atomisation conditions investigated here (Fig. 8b). It should be noted that the values of S_{u} reported are stretched values. Thus, effects of non-equidiffusive conditions at the flame front can be expected to increase the effect of stretch on the measured S_{b} in the present jet fuel-air flames, especially due to the relative small size of the flame kernels. The raw measurements of the burnt flame speed S_{b} as well as

the calculated densities of the burnt gases and fresh mixture used to evaluate S_u are given in Table 5 of the Appendix.

In addition, flame speeds higher than the estimated turbulent burning velocity were verified in these experiments. The flame speed measurements were normalised in terms of the gaseous turbulent burning velocity, which was calculated based on the laminar burning velocity and the correlation proposed in [48]. For that, the respective parameters of the mixture and the flow were considered at each test condition. These results are shown in Fig. 8 in terms of (c) SMD and (d) $u'_z/S^\circ_{\mathrm{L},g}$. Flame speeds higher than $S_{\mathrm{T,g}}$ were observed for most of conditions with $\phi = 1.4$, with the highest absolute values being at fine atomisation conditions (d_{32}=16-22 μm). Other than the flame propagating at an effective equivalence ratio different from the overall value, the presence of droplets inside the flame has been observed to contribute to the high flame speed values found in previous DNS works [16, 20]. This phenomenon is visualised and discussed further in Sec. 3.3. Additionally, a slight increase of $\overline{S}_\mathrm{u}$ with SMD (Fig. 8a,c) was present under lean conditions for both fuels, as opposed to the negative correlation found under stoichiometric and rich conditions. This positive effect of large droplets was verified even though $u'_z/S^\circ_{\mathrm{L},g}$ decreased with SMD (Fig. 8d). This has also been observed in other experimental works, which attributed to the inhomogeneities caused by large droplets, facilitating the flame propagation [11].

Another important observation is that the measured flame speed in all lean conditions was distinctly low and similar to the laminar burning velocity at the lower flammability limit (Fig. 8b). The present results illustrate different ways in which flame speed enhancement may take place, in relation to a gaseous mixture or even a finer spray, for example. In Sec. 3.3, the mechanisms of flame propagation are discussed in detail through direct observations of the ignition event, offering visual evidence to explain the behaviours observed in Fig. 8.

Figure 9 shows the main characteristics of typical spray flames for the range of conditions studied. Jet A flames at 1 ms after the spark are shown through (a) OH* and (b) schlieren visualisation, with coarse (d_{32}=33 μm) and fine (d_{32}=16 μm) atomisation cases shown at the top and bottom rows, respectively, and ϕ of 0.8, 1, and 1.4 from left to right. The visualisation area shown for each flame is exactly the same between the OH* and the schlieren image, with the latter being flipped, or mirrored, in relation to its vertical axis for convenience. Also, as noted previously, the visualisation settings

were kept the same during all experiments, hence the OH* signal can be directly compared between conditions.

The difference between fine and coarse atomisation can be seen in the schlieren images of Fig. 9b. The small black dots in the image represent the shadowgraph of large droplets in the flow (top row), while only a homogenous grey region can be seen where a monodisperse-like spray was obtained and droplets cannot be individually identified (bottom row). The presence of a polydisperse spray with high SMD gave rise to pockets of strong heat release in the flame. These are likely large individually burning droplets, as the presence of liquid fuel in that region was confirmed through PLIF visualisation. In contrast, a high heat release concentration was found in elongated regions of the flow with length of the order of L_{11}. This characteristic suggests that the highly dense OH* regions could be related to reaction occurring in clusters of droplets, as droplets with Stokes number around unity tend to accumulate due to turbulence [49]. It should be noted that such wrinkled structures were hardly found in the PLIF images due to their three-dimensional character.

3.3. Flame propagation mechanisms

Three distinct flame propagation modes were observed in the present experiments. The first was characterised by a homogenous gaseous-like flame front, which also exhibited aspects of the sheath combustion mode described in [22]. The second propagation mode was characterised by strong reaction occurring only around large droplets. Finally, the third mode lied in between the two others, exhibiting a homogenous heat release across the flame but also some zones of high heat release around large droplets. The first propagation mode is referred to as gaseous-like mode throughout this text, while the second and third mode fit the description of the droplet and inter-droplet propagation modes given by Neophytou et al. [20] in their DNS work, thus the same terms are used.

3.3.1. Droplet propagation mode

This mode was characteristic of lean mixtures with SMD between 16-33 μm. In Fig 10, an OH* line-of-sight image sequence illustrates a typical event exhibiting droplet-propagation mode (a). The role of fuel droplets in such mode can be better understood through the OH/fuel PLIF sequence of an additional event show in (b). In the PLIF images, the OH signal is shown in colour and the cubic root of the fuel fluorescence signal (representing the

droplet diameter) is shown in a grey scale. It should be noted that the fuel fluorescence signal being imaged is mostly from the liquid phase due to a much higher molecular number density in comparison to the gas phase. Also, due to the relatively low signal of small droplets combined to the image resolution, the smallest droplets seen in the image have an approximate size of 10-30 μm, estimated as the same order of magnitude of the sensor pixel. To allow the visualisation of very low heat release zones in (a), the OH* colour map was rescaled to a logarithmic form specifically in this propagation mode.

The propagation of the flame occurred preferentially through bridges between large droplets or groups of droplets, similarly to the propagation mechanism observed in a stroichioimetric 20-μm monodisperse spray of n-heptane [20]. Although the line-of-sight character of OH* experiments makes it difficult for a precise assessment of the flame front (Fig 10a), burning droplets seemed to have allowed for the local advancement the flame front towards the fresh mixture, which in turn ignited new large droplets. This can also be seen in the PLIF sequence (Fig 10b), where the flame front can be understood to lie at the leading edge of the OH-dense region, between this and the droplet field. In these regions, the flame front seemed to propagate faster than the average front, suddenly engulfing parts of the flow.

In the experiments, the propagating front surrounding the large burning droplets exhibited an especially low OH* signal, approximately ten times lower than in the vicinity of a droplet, indicating significant fuel deprivation and low heat release in those areas. Additionally, local extinction was observed in parts of the flame front lacking the presence of large individually burning droplets. These localised sources of heat release have been verified in DNS to allow for the reaction even in below-flammable inter-droplet gas phase [20], which seems to be the phenomenon taking place in Fig 10a. However, in contrast to DNS [20], droplet-mode propagation occurred only at ϕ of 0.8 for a similar d_{32}. This is likely associated to the prevaporised fuel present in the inter-droplet space ($\phi_g = 0.3$), in addition to numerous small droplets in the 1-10 μm range, which should present fast evaporation time scales. It should be noted that in a polydisperse spray, the amount of fuel accumulated in droplets smaller than what can be clearly resolved by the camera sensor (d<15 μm), being most of the droplets in the flow, accounted for roughly 25% of the liquid fuel. Hence, considering the prevaporised fuel in the gas phase, large and scarce droplets must have accounted for approximately half of the energy released through combustion.

Moreover, the overall ignition of the flame was strongly attributed to the

presence a few large droplets at the location of the spark, verified in the first few frames of the event. Typically, immediate quenching of the flame was verified in events that did not exhibited individually burning droplets following the spark. As verified in DNS of sprays [16, 17] and stratified gaseous mixtures [50], mixture inhomogeneities may facilitate the reaction in regions of optimal equivalence ratio, consequently enhancing the overall ignition of the flame. Thus, the slight increase in flame speed with SMD observed for both Jet A and ATJ-8 (Fig. 8a) may be associated with this mechanism.

3.3.2. Inter-droplet propagation mode

For sprays in the 21-33 μm SMD range, the heat release across the flame was significantly more homogenous in stoichiometric to rich mixtures (Fig. 11a) than in lean mixtures characterised by the droplet propagation mode (Fig. 10a). This effect seemed to be a consequence of fast evaporation rates found close to the flame front, as suggested by the PLIF sequence (Fig. 11b) with droplets quickly disappearing as they approached the flame. Consequently, a less stratified inter-droplet region is expected, richer than in overall lean mixtures with the same droplet sizes.

Further, the expansion of the flame pushed small droplets in its vicinity away towards its propagation direction, eventually leading to their full evaporation. Yet, large droplets survived the propagating front likely due to their higher momentum, evaporating significantly close to the flame front and producing small regions of high curvature. As a result, OH* inhomogeneities was verified across the flame, likely around large droplets penetrating the flame or in regions where full droplet vaporisation occurred at the flame front. This effect is less visible for ATJ-8 (Fig. 11a), but is clearly seen in Jet A (Fig. 9a) for the same condition (ϕ=1.4, d_{32}=33 μm). Nevertheless, the OH* signal was still generally higher and more uniform than for droplet-propagation cases. These observations are, again, consistent with previous DNS works [16, 20, 28], and describe the inter-droplet ignition mode as defined in [20].

Interestingly, some of the largest droplets in the flow fully penetrated the flame front reaching the centre of the burnt gases, where they continued to evaporate. Typically, this type of phenomenon is observed in spray flames where large droplets are ballistic, due to the high momentum provided by the atomisation nozzle, which may cause local extinction of the flame [31]. In the present experiments, this phenomenon is attributed to the slow evaporation timescale of the droplets compared to the front speed due to the fuel's low

volatily. Moreover, although a precise evaluation of the change in droplet size is not feasible in PLIF studies due to potential out-of-plane motion, the dark regions surrounding the droplets inside the flame indicate the lack of OH as a consequence of a high concentration of fuel vapour. Due to high evaporation rates induced by the high temperatures found inside the flame, combustion products including OH were likely pushed away from the droplets due to a Stefan flow. The OH-poor regions slowly disappeared, indicating a fast diffusion process of fuel within the burnt products. This phenomenon has been used to explain the unusually high flame speeds that can be found in spray flame. The diffusion of fuel in the products side towards the reaction zone [16] and its possible pyrolysis due to the high combustion temperatures [20] are two possible contributions. Still, the highest flame speeds in the present experiments (Fig. 8) were found for conditions where full vaporisation occurred ahead of the flame, as described in the next section.

Characteristic curvatures concerning two individual events for each fuel at the above-mentioned flow conditions are presented in Fig. 12, with the shape of the flame front shown in (a) and its respective curvature probability density function (pdf) in (b). The flames exhibited the characteristic toroidal shape of laser ignition, arising from the fact that the centre of propagation of the shock-wave following the spark is slightly shifted up the laser beam relative to the centroid of the breakdown plasma, as discussed in [51]. Propagation occurred at a wide range of curvature values, with virtually no difference between the two fuels. A preferential positive curvature value of approximately $0.2\,\mathrm{mm}^{-1}$ was found at 1.35 ms after the spark, that is, corresponding to approximately the mean radius of the flame. Still, a significant portion of the flame propagated at negative curvature values, which were attributed to the presence of droplets and turbulence. As a result of this effect, an asymmetric pdf was observed, which differ from findings in gaseous turbulent premixed flames [52, 53]. The presence of negative curvatures have also been observed in DNS of spray flames both in laminar and turbulent conditions ($S_\mathrm{u}/S^\circ_{\mathrm{L,g},\phi=1}$=0–8; $G \gg 1$; d/δ_f =0.02–0.06) [18, 19]. Although turbulence may mask the contribution of droplets to flame curvature, a clear widening of the curvature pdfs as turbulence increased has been noticed in [18]. This effect can be identified directly in the present experiments by looking at a large droplet approaching the flame front, as shown in Fig. 13. The position of the flame front as well as the fuel droplets at three distinct moments are shown in Fig. 13a, with the respective flame curvature pdf for the region of the flame isolated in (a) is shown in (b). Significant wrinkling

of the flame occurred as the large droplet approached the flame, resulting in a wide range of negative curvature values and a decrease of the preferential curvature value of the flame found in the probability density function.

3.3.3. Gaseous-like propagation mode

From the inter-droplet propagation mode, decreasing the SMD of the rich spray further to 16 μm led to flame propagation in a gaseous-like fashion (Fig. 14). At this condition, virtually all droplets evaporated far from the flame, giving rise to a thick and fully gaseous layer between the spray and the flame front (Fig. 14b), similarly to what is found in sheath combustion mode for high G [22]. A regime diagram for the range of experimental conditions and their respective Group number is given in Fig. 15, with the sheath-combustion line (G=10^2) [22] added for reference. Further, due to evaporation occurring far ahead of the flame, the gaseous-like propagation mode exhibited the highest and most homogenous OH* levels (Fig. 14a) within the range of experimental conditions. Evidence from DNS results of [18] has shown that, for similar conditions, such increase in heat release occurring as droplet sizes decrease is a direct consequence of predominantly premixed-type reactions as opposed to predominantly non-premixed; the latter occurring in cases similar to the presented droplet-propagation regimes. Further, in a few events, scarce large droplets were observed in the gaseous layer, nearly reaching the flame. However, full penetration of such droplets across the flame was not observed, with full evaporation occurring within roughly 600 μs once the droplets entered the gaseous layer. This effect is also reflected in the curvature plots, as propagation at a slightly wider range of curvatures was observed in relation to the inter-droplet mode, with the pdfs exhibiting a more symmetric shape (Fig. 16).

4. Conclusions

This work presented a direct experimental visualisation of the propagation mechanisms of spray flames. OH* chemiluminescence, schlieren, and simultaneous OH/fuel PLIF imaging were used to visualise the ignition and development of spherically expanding flames in uniformly distributed polydisperse droplets in a turbulent jet. Three distinct propagation modes were identified: the droplet, inter-droplet, and gaseous-like propagation modes.

The droplet-propagation mode, typical of lean mixtures (ϕ=0.8, SMD 16-33 μm), was characterised by concentrated reactions around large droplets

or groups of droplets immediately following the spark. These individually burning droplets allowed for the local propagation of a flame front marked by considerably low heat release levels. Thus, successful ignition of the flame kernel relied on the propagation of this front to ignite new large droplets in its vicinity. In the absence of individually burning droplets, local extinction was found. These observations are in agreement with DNS, confirming the presence of a slowly propagating flame front due to reaction occurring in below-flammable inter-droplet space even at times greater than the duration of the spark effects on the flame. Significantly low flame speeds of roughly 0.1 m/s were verified in such conditions. Still, a slight increase of flame speed with SMD was observed both in Jet A and ATJ-8 fuels, possibly due to the enhancement of small-scale mixture inhomogeneities arising from a more polydisperse spray.

A more vigorous and uniform flame front was found in stoichiometric to rich conditions (ϕ=1-1.4, SMD 16-27 μm) as a result of increased evaporation of the droplets ahead of the flame. In this inter-droplet propagation mode, a negative correlation of flame speed with SMD was observed, with ATJ-8 presenting faster flame speeds than ATJ-8 at ϕ of 1.4 and high SMD. Further, the behaviour of flame speed with SMD at stoichiometric to rich conditions is expected due to the decrease of the surface area of the spray, being detrimental to evaporation. Nonetheless, the measured flame speed values were noticeably higher than the laminar burning velocity of the counterpart gaseous mixture. The unusually high flame speeds have been observed in DNS and associated with an additional influx of pyrolysed fuel from droplets that penetrate the flame. In the experiments, evaporation of the droplets and diffusion of fuel within the burnt products were also observed, corroborating the numerical findings. Additionally, negative droplet-induced curvature values were observed as droplets approached the flame, while large droplets fully penetrated through the flame.

Finally, the highest flame speeds were observed once the SMD decreased to 16 µm in the rich spray (ϕ=1.4), leading to a dense spray and the gaseous-like propagation mode. A suppression of the droplet-induced effects (i.e. wrinkling and penetration) was verified, giving rise to a fully gaseous layer ahead of the flame and, therefore, a flame front more commonly found in propagation in very fine mists or sprays of volatile fuels such as ethanol.

Acknowledgements

P.M. de Oliveira is grateful for the financial support of the Brazilian Space Agency and Brazil's National Council for Scientific and Technological Development. This work has also been partly funded by the European Commission Clean Sky 2 project PROTEUS (785349). The authors acknowledge Dr. G. Nivarti for the fruitful discussions, M.P. Sitte for his help with the flame propagation calculations, and Drs. P.M. Allison and A.W. Skiba for their assistance with the visualisation techniques. Also, the authors thank Drs. M.B. Colket and J.S. Heyne for the collaboration with the United States' National Jet Fuel Combustion Program, and Dr. J.T. Edwards at the U.S. Air Force Research Laboratory for kindly providing the fuels.

References

[1] J. H. Burgoyne, L. Cohen, The Effect of Drop Size on Flame Propagation in Liquid Aerosols, Proc. R. Soc. A Math. Phys. Eng. Sci. 225 (1954) 375–392.

[2] E. K. Čekalin, Propagation of flame in turbulent flow of two-phase fuel-air mixture, Symp. (Int.) Combust. 8 (1961) 1125–1129.

[3] Y. Mizutani, T. Nishjmoto, Turbulent Flame Velocities in Premixed Sprays Part I. Experimental Study, Combust. Sci. Technol. 6 (1972) 1–10.

[4] Y. Mizutani, A. Nakajima, Combustion of fuel vapor-drop-air systems: Part IISpherical flames in a vessel, Combust. Flame 20 (1973) 351–357.

[5] Y. Mizutani, A. Nakajima, Combustion of fuel vapor-drop-air systems: Part I-Open burner flames, Combust. Flame 20 (1973) 343–350.

[6] C. E. Polymeropoulos, S. Das, The effect of droplet size on the burning velocity of kerosene-air sprays, Combust. Flame 25 (1975) 247–257.

[7] S. Hayashi, S. Kumagai, T. Sakai, Propagation Velocity and Structure of Flames in Droplet-Vapor-Air Mixtures, Combust. Sci. Technol. 15 (1977) 169–177.

[8] D. R. Ballal, A. H. Lefebvre, Flame propagation in heterogeneous mixtures of fuel droplets, fuel vapor and air, Symp. (Int.) Combust. 18 (1981) 321–328.

[9] G. D. Myers, A. H. Lefebvre, Flame propagation in heterogeneous mixtures of fuel drops and air, Combust. Flame 66 (1986) 193–210.

[10] G. A. Richards, A. H. Lefebvre, Turbulent flame speeds of hydrocarbon fuel droplets in air, Combust. Flame 78 (1989) 299–307.

[11] H. Nomura, I. Kawasumi, Y. Ujiie, J. Sato, Effects of pressure on flame propagation in a premixture containing fine fuel droplets, Proc. Combust. Inst. 31 II (2007) 2133–2140.

[12] M. Lawes, A. Saat, Burning rates of turbulent iso-octane aerosol mixtures in spherical flame explosions, Proc. Combust. Inst. 33 (2011) 2047–2054.

[13] D. R. Ballal, A. H. Lefebvre, Ignition and flame quenching of flowing heterogeneous fuel-air mixtures, Combust. Flame 35 (1979) 155–168.

[14] C. E. Polymeropoulos, Flame Propagation in Aerosols of Fuel Droplets, Fuel Vapor and Air, Combust. Sci. Technol. 40 (1984) 217–232.

[15] Y. Mizutani, M. Ogasaware, Laminar flame propagation in droplet suspension of liquid fuel, Int. J. Heat Mass Transf. 8 (1965) 921–935.

[16] A. P. Wandel, N. Chakraborty, E. Mastorakos, Direct numerical simulations of turbulent flame expansion in fine sprays, Proc. Combust. Inst. 32 (2009) 2283–2290.

[17] A. Neophytou, E. Mastorakos, R. S. Cant, DNS of spark ignition and edge flame propagation in turbulent droplet-laden mixing layers, Combust. Flame 157 (2010) 1071–1086.

[18] G. O. Erol, J. Hasslberger, M. Klein, N. Chakraborty, A direct numerical simulation analysis of spherically expanding turbulent flames in fuel droplet-mists for an overall equivalence ratio of unity, Phys. FLuids 30 (2018).

[19] G. O. Erol, J. Hasslberger, M. Klein, N. Chakraborty, A Direct Numerical Simulation investigation of spherically expand- ing flames propagating in fuel droplet-mists for different droplet diameters and overall equivalence ratios, Combust. Sci. Technol. (2019) 1–49.

[20] A. Neophytou, E. Mastorakos, R. S. Cant, The internal structure of igniting turbulent sprays as revealed by complex chemistry DNS, Combust. Flame 159 (2012) 641–664.

[21] P. M. de Oliveira, P. M. Allison, E. Mastorakos, Ignition of uniform droplet-laden weakly turbulent flows following a laser spark, Combust. Flame 199 (2019) 387–400.

[22] H. H. Chiu, T. M. Liu, Group Combustion of Liquid Droplets, Combust. Sci. Technol. 17 (1977) 127–142.

[23] E. Mastorakos, Forced ignition of turbulent spray flames, Proc. Combust. Inst. 36 (2017) 2367–2383.

[24] S. Aggarwal, A review of spray ignition phenomena: Present status and future research, Prog. Energy Combust. Sci. 24 (1998) 565–600.

[25] J. L. Beduneau, N. Kawahara, T. Nakayama, E. Tomita, Y. Ikeda, Laser-induced radical generation and evolution to a self-sustaining flame, Combust. Flame 156 (2009) 642–656.

[26] C. Cardin, B. Renou, G. Cabot, A. M. Boukhalfa, Experimental analysis of laser-induced spark ignition of lean turbulent premixed flames: New insight into ignition transition, Combust. Flame 160 (2013) 1414–1427.

[27] R. Thimothée, C. Chauveau, F. Halter, C. Nicoli, P. Haldenwang, B. Denet, Microgravity experiments and numerical studies on ethanol/air spray flames, Comptes Rendus - Mec. 345 (2017) 99–116.

[28] D. H. Wacks, N. Chakraborty, E. Mastorakos, Statistical Analysis of Turbulent Flame-Droplet Interaction: A Direct Numerical Simulation Study, Flow, Turbul. Combust. 96 (2016) 573–607.

[29] C. Nicoli, P. Haldenwang, B. Denet, Spray-Flame Dynamics in a Rich Droplet Array, Flow, Turbul. Combust. 96 (2016) 377–389.

[30] D. Bradley, M. Lawes, S. Liao, A. Saat, Laminar mass burning and entrainment velocities and flame instabilities of i-octane, ethanol and hydrous ethanol/air aerosols, Combust. Flame 161 (2014) 1620–1632.

[31] A. Verdier, J. Marrero Santiago, A. Vandel, G. Godard, G. Cabot, B. Renou, Local extinction mechanisms analysis of spray jet flame using high speed diagnostics, Combust. Flame 193 (2018) 440–452.

[32] A. P. Wandel, Influence of scalar dissipation on flame success in turbulent sprays with spark ignition, Combust. Flame 161 (2014) 2579–2600.

[33] P. M. de Oliveira, E. Mastorakos, Effects of droplet size on the ignition of conventional and alternative jet fuels in turbulent air, in: 9th Int. Symp. Turbul. Heat Mass Transf., Rio de Janeiro, 2018.

[34] P. M. de Oliveira, E. Mastorakos, The structure of spherical flames in turbulent two-phase flows as revealed by OH and fuel PLIF, in: AIAA Scitech 2019 Forum, American Institute of Aeronautics and Astronautics, Reston, Virginia, 2019. URL: https://arc.aiaa.org/doi/10.2514/6.2019-2243. doi:10.2514/6.2019-2243.

[35] J. T. Edwards, Reference Jet Fuels for Combustion Testing, in: 55th AIAA Aerosp. Sci. Meet., American Institute of Aeronautics and Astronautics, Reston, 2017. URL: http://arc.aiaa.org/doi/10.2514/6.2017-0146. doi:10.2514/6.2017-0146.

[36] M. Colket, J. Heyne, M. Rumizen, M. Gupta, T. Edwards, W. M. Roquemore, G. Andac, R. Boehm, J. Lovett, R. Williams, J. Condevaux, D. Turner, N. Rizk, J. Tishkoff, C. Li, J. Moder, D. Friend, V. Sankaran, Overview of the National Jet Fuels Combustion Program, AIAA J. 55 (2017) 1087–1104.

[37] K. Wang, R. Xu, T. Parise, J. Shao, A. Movaghar, D. J. Lee, J. W. Park, Y. Gao, T. Lu, F. N. Egolfopoulos, D. F. Davidson, R. K. Hanson, C. T. Bowman, H. Wang, A physics-based approach to modeling real-fuel combustion chemistry IV. HyChem modeling of combustion kinetics of a bio-derived jet fuel and its blends with a conventional Jet A, Combust. Flame 193 (2019) 520–537.

[38] M. Orain, P. Baranger, C. Ledier, J. Apeloig, F. Grisch, Fluorescence spectroscopy of kerosene vapour at high temperatures and pressures: Potential for gas turbines measurements, Appl. Phys. B Lasers Opt. 116 (2014) 729–745.

[39] Y. Hardalupas, M. Orain, Local measurements of the time-dependent heat release rate and equivalence ratio using chemiluminescent emission from a flame, Combust. Flame 139 (2004) 188–207.

[40] F. N. Egolfopoulos, N. Hansen, Y. Ju, K. Kohse-Höinghaus, C. K. Law, F. Qi, Advances and challenges in laminar flame experiments and implications for combustion chemistry, Prog. Energy Combust. Sci. 43 (2014) 36–67.

[41] COSILAB, Cosilab collection, v3.3.2, Rotexo-Softpredict-Cosilab GmbH and Co. KG Bad Zwischenahn (Germany), 2012.

[42] P. Dagaut, On the kinetics of hydrocarbons oxidation from natural gas to kerosene and diesel fuel, Phys. Chem. Chem. Phys. 4 (2002) 2079–2094.

[43] G. P. Smith, D. M. Golden, M. Frenklach, N. W. Moriarty, B. Eiteneer, M. Goldenberg, C. T. Bowman, R. K. Hanson, S. Song, W. C. Gardiner Jr., V. V. Lissianski, Z. . Qin, GRI-Mech 3.0, http://www.me.berkeley.edu/gri_mech/, ????

[44] C. M. Vagelopoulos, F. N. Egolfopoulos, Direct experimental determination of laminar flame speeds, Symp. (Int.) Combust. 27 (1998) 513–519.

[45] Z. Chen, M. P. Burke, Y. Ju, Effects of Lewis number and ignition energy on the determination of laminar flame speed using propagating spherical flames, Proc. Combust. Inst. 32 (2009) 1253–1260.

[46] N. K. Rizk, A. H. Lefebvre, Drop-size distribution characteristics of spill-return atomizers, J. Propuls. Power 1 (1985) 16–22.

[47] R. Moffat, Describing the uncertainties in experimental results, Exp. Therm. Fluid Sci. 1 (1988) 3–17.

[48] D. Bradley, How fast can we burn?, Symp. (Int.) Combust. (1992) 247–262.

[49] J. K. Eaton, J. R. Fessler, Preferential concentration of particles by turbulence, Int. J. Multiph. Flow 20 (1994) 169–209.

[50] N. Chakraborty, E. Mastorakos, Direct numerical simulations of localised forced ignition in turbulent mixing layers: The effects of mixture fraction and its gradient, Flow, Turbul. Combust. 80 (2008) 155–186.

[51] D. Bradley, C. G. W. Sheppard, I. M. Suardjaja, R. Woolley, Fundamentals of high-energy spark ignition with lasers, Combust. Flame 138 (2004) 55–77.

[52] S. Gashi, J. Hult, K. W. Jenkins, N. Chakraborty, S. Cant, C. F. Kaminski, Curvature and wrinkling of premixed flame kernels comparisons of OH PLIF and DNS data, Proc. Combust. Inst. 30 (2005) 809–817.

[53] A. Alqallaf, M. Klein, N. Chakraborty, Effects of Lewis Number on the Evolution of Curvature in Spherically Expanding Turbulent Premixed Flames, Fluids 4 (2019) 17–27.

Appendix

Table 5 presents the measured values of burnt flame speed S_b (i.e., the speed at which the flame front propagates relative to the lab coordinates) as well as the densities of the burnt products and of the reactants. These were used to estimate the values of stretched unburnt flame speed through Eq. 2, which are reported in Fig. 8 for all the experimental conditions of this work.

Table 5: Measured values of the burnt flame speed, and respective values of burnt and unburnt densities obtained from 1-D calculations used to evaluate the unburnt flame speed.

	Jet A		ATJ-8		1-D calc.	
ϕ	d_{32}	S_b	d_{32}	S_b	ρ_b	ρ_u
(-)	(μm)	(m/s)	(μm)	(m/s)	(kg/m^3)	(kg/m^3)
0.8	33	0.58	33	0.83	0.161	1.02
0.8	27	0.47	28	0.62		
0.8	23	0.47	23	0.73		
0.8	16	0.33	16	0.54		
1.0	32	1.01	34	1.26	0.148	1.03
1.0	28	1.13	29	1.09		
1.0	21	1.29	23	1.47		
1.0	17	1.86	16	1.58		
1.4	33	2.07	33	3.20	0.152	1.05
1.4	27	2.68	28	3.69		
1.4	21	3.61	23	3.83		
1.4	16	3.80	17	3.79		

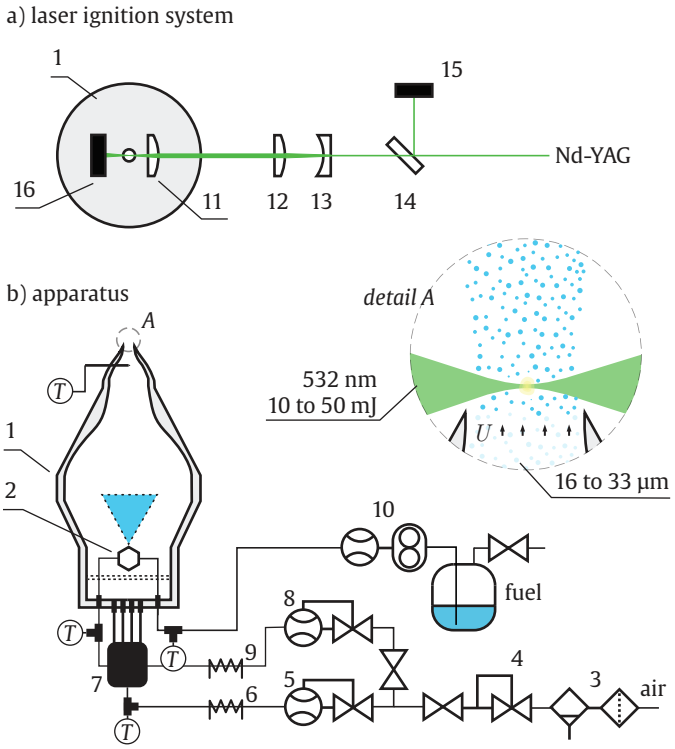

Figure 1: Schematic representation of (a) the apparatus and (b) the laser ignition system. The components of the system are: (1) burner, (2) air-assist atomiser, (3) particulate and coalescent filters, (4) pressure regulator, (5,8) flow controller, (6,9) in-line heater, (7) flow splitter, (10) Coriolis flow meter and gear pump, (11) 30-mm plano-convex lens, (12) 75-mm plano-convex lens, (13) -30-mm plano-concave lens, (14) beam-splitter, (15,16) pyroelectric energy meters. Modified from [21].

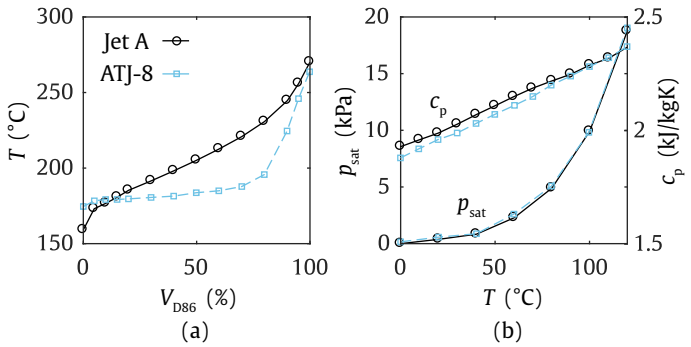

Figure 2: (a) ASTM D86 distillation curve and (b) vapour pressure and heat capacity of Jet A and ATJ-8. Data obtained from [35].

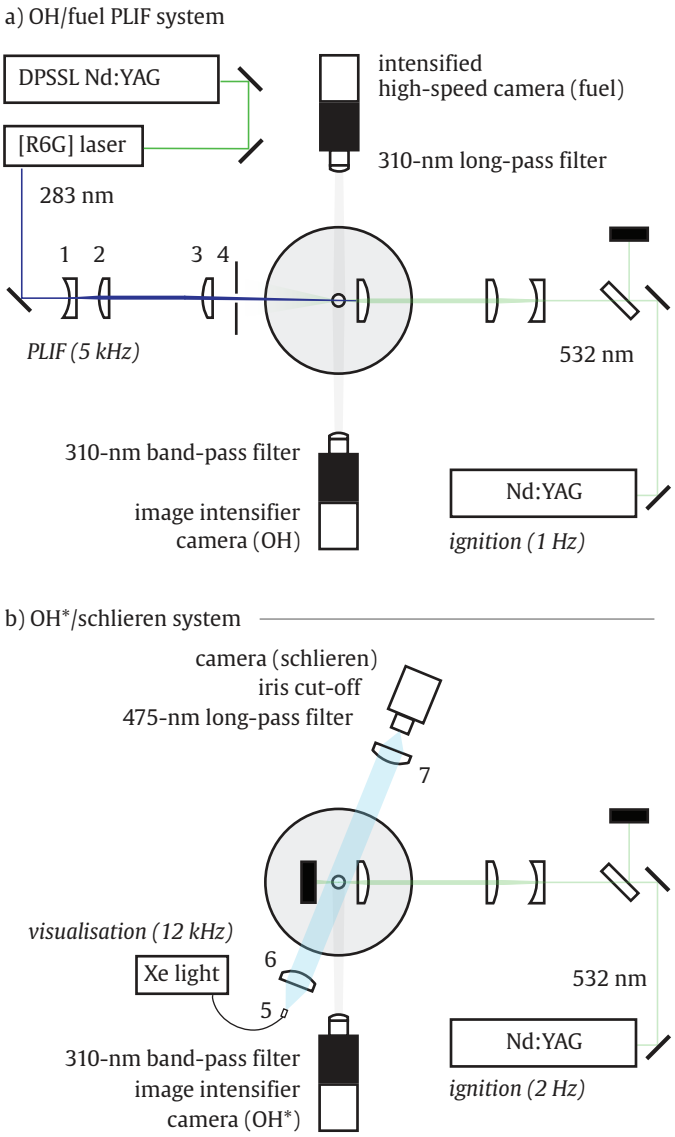

Figure 3: Schematic representation of the (a) OH/fuel planar laser-induced fluorescence setup and (b) OH*-chemiluminescence and schlieren setup. The components of the system are: (1) 100-mm plano-convex cylindrical lens, (2) -30-mm plano-concave cylindrical lens, (3) 20-mm plano-convex cylindrical lens, (4) cut-off plate, (5) 1-mm optical fiber, (6) 200-mm plano-convex lens, (7) 500-mm plano convex lens.

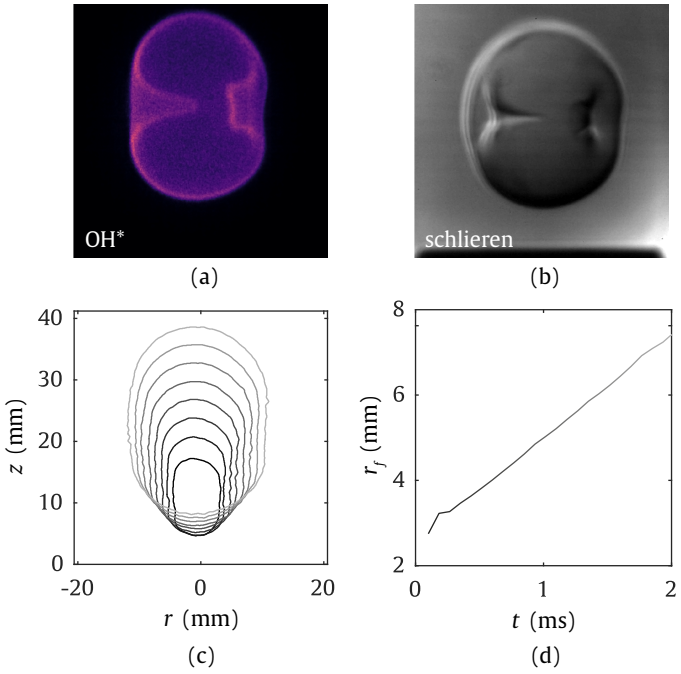

Figure 4: Instantaneous (a) OH* and (c) schlieren image of the methane premixed flame at 2 ms after the spark. The evolution of the (c) shape and (d) radius of the flame calculated from the OH* image sequence in a single ignition event is also shown – $E_{in} = 60\,\mathrm{mJ}$, $\phi = 1.1$.

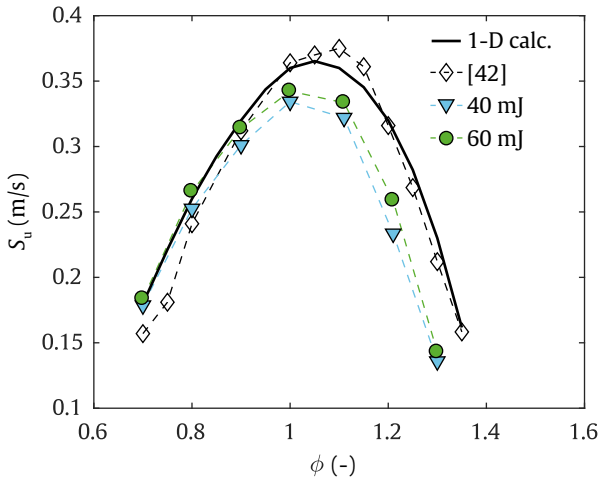

Figure 5: Comparison of experimental measurements of S_u carried out in a laminar methane-air jet against one-dimensional calculations using Cosilab and [43], and experimental data of Vagelopoulos & Egolfopoulos (1998) [44].

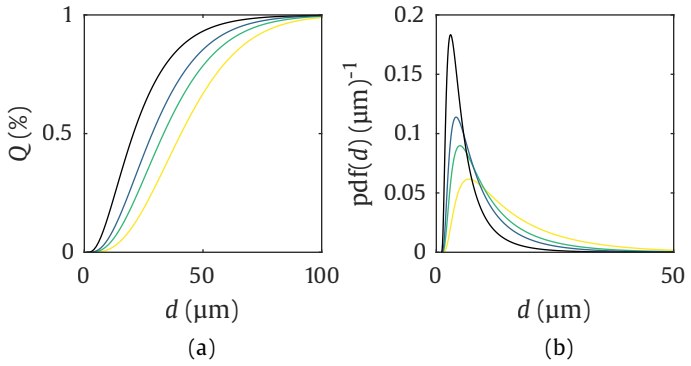

Figure 6: Example of Rosin-Rammler distributions of (a) accumulated volume and (b) pdf of droplet size for four degrees of atomisation – ATJ-8, ϕ=0.8.

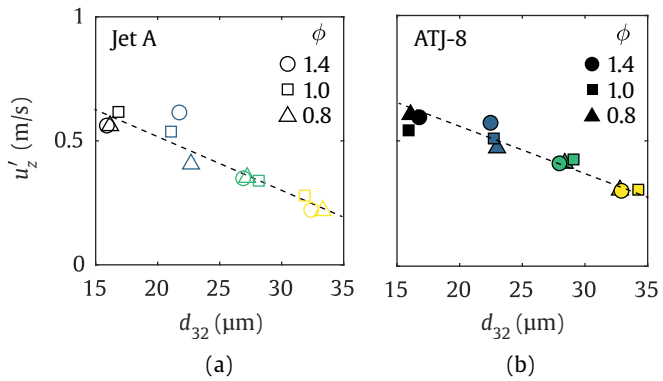

Figure 7: Resulting axial velocity rms fluctuation in terms of the spray SMD for (a) Jet A and (b) ATJ-8.

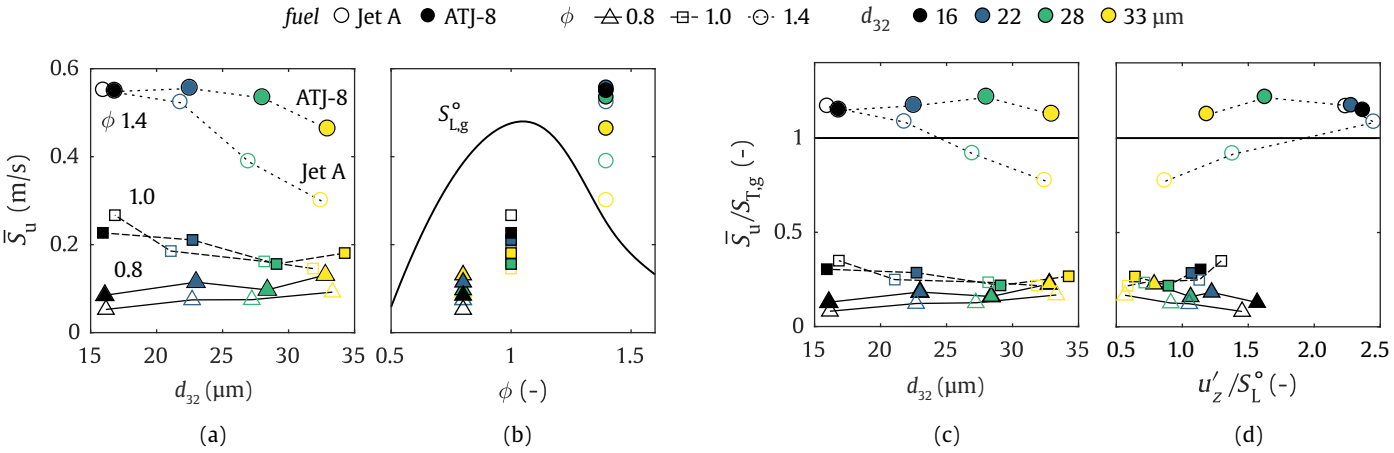

Figure 8: Effect of droplet size on the measured unburnt flame speed of (a) Jet A and ATJ-8. A comparison against the gaseous laminar burning velocity of a 1-D gaseous premixed flame using the Dagaut chemical mechanism [42] is shown in (b). The measurements in (a) were normalised in terms of the gaseous turbulent burning velocity calculated using Bradley's correlation [48] and are shown in terms of the (c) SMD and (d) $u'_z/S_{\mathrm{L,g}}$.

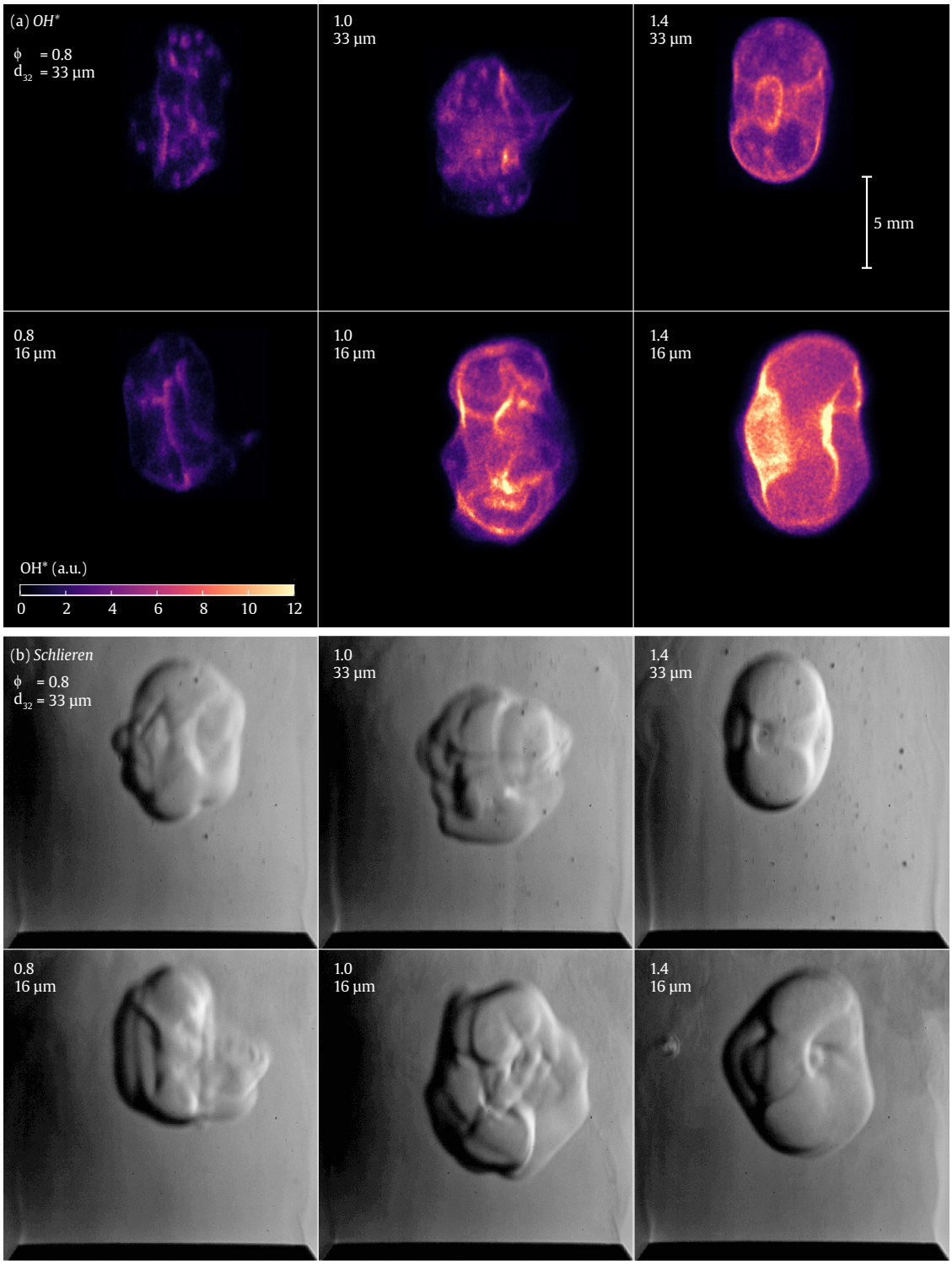

Figure 9: Simultaneous (a) OH* and (b) schlieren snapshots of characteristic Jet A flames 1 ms after the spark. Based on [33].

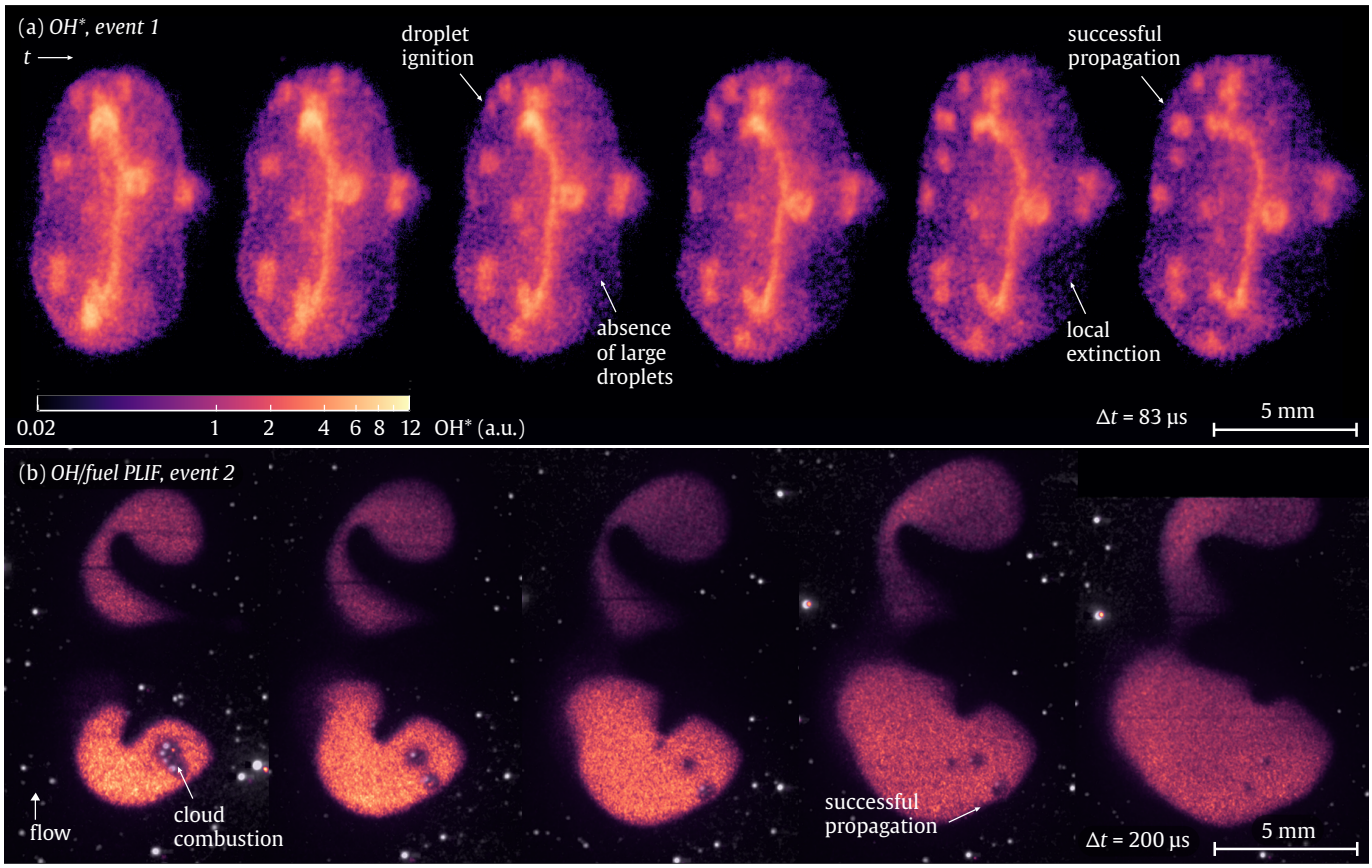

Figure 10: Examples of droplet propagation mode visualised by (a) OH* and (b) OH/fuel PLIF – Jet A, ϕ=0.8, d_{32}=33 µm. OH* signal in (a) is shown in a logarithmic scale revealing the low heat-release zones.

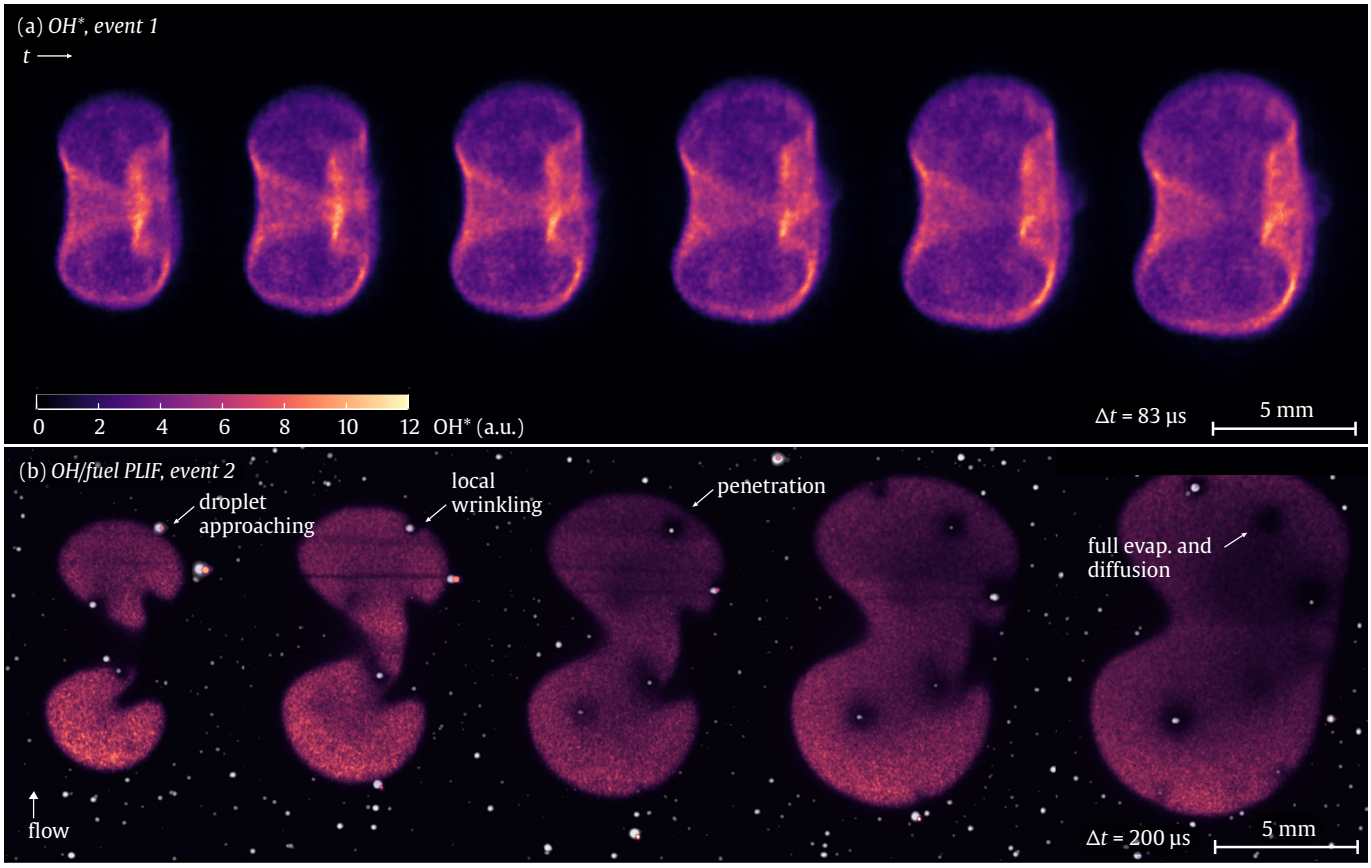

Figure 11: Examples of inter-droplet propagation mode visualised by (a) OH* and (b) OH/fuel PLIF – ATJ-8, ϕ=1.4, d_{32}=33 µm.

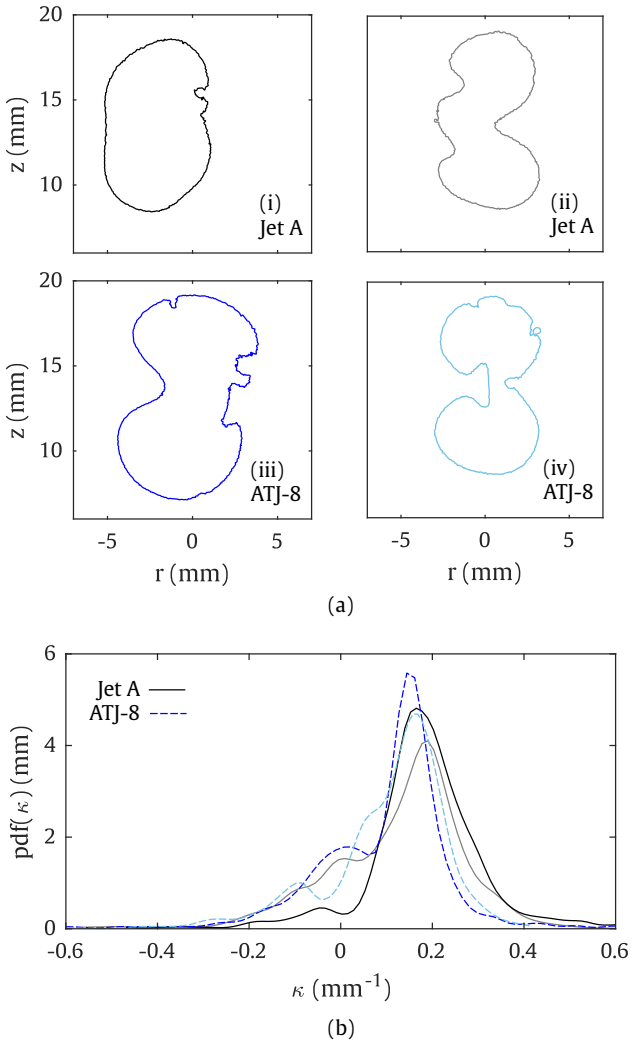

Figure 12: Shape of the flames (a) and respective curvature pdfs (b) for Jet A and ATJ-8 at 1.35 ms after the spark – ϕ=1.4, d_{32}=33 µm.

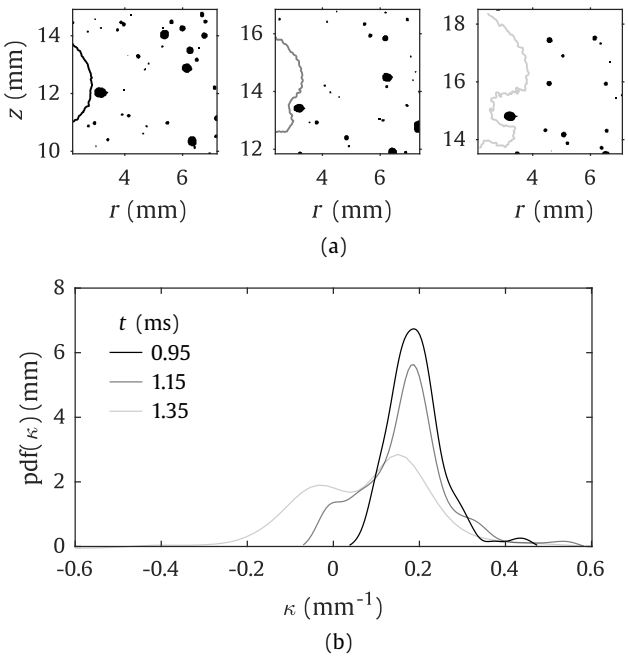

Figure 13: Effect of droplet penetration on the flame curvature – ATJ-8, ϕ=1.4, d_{32}=33 µm.

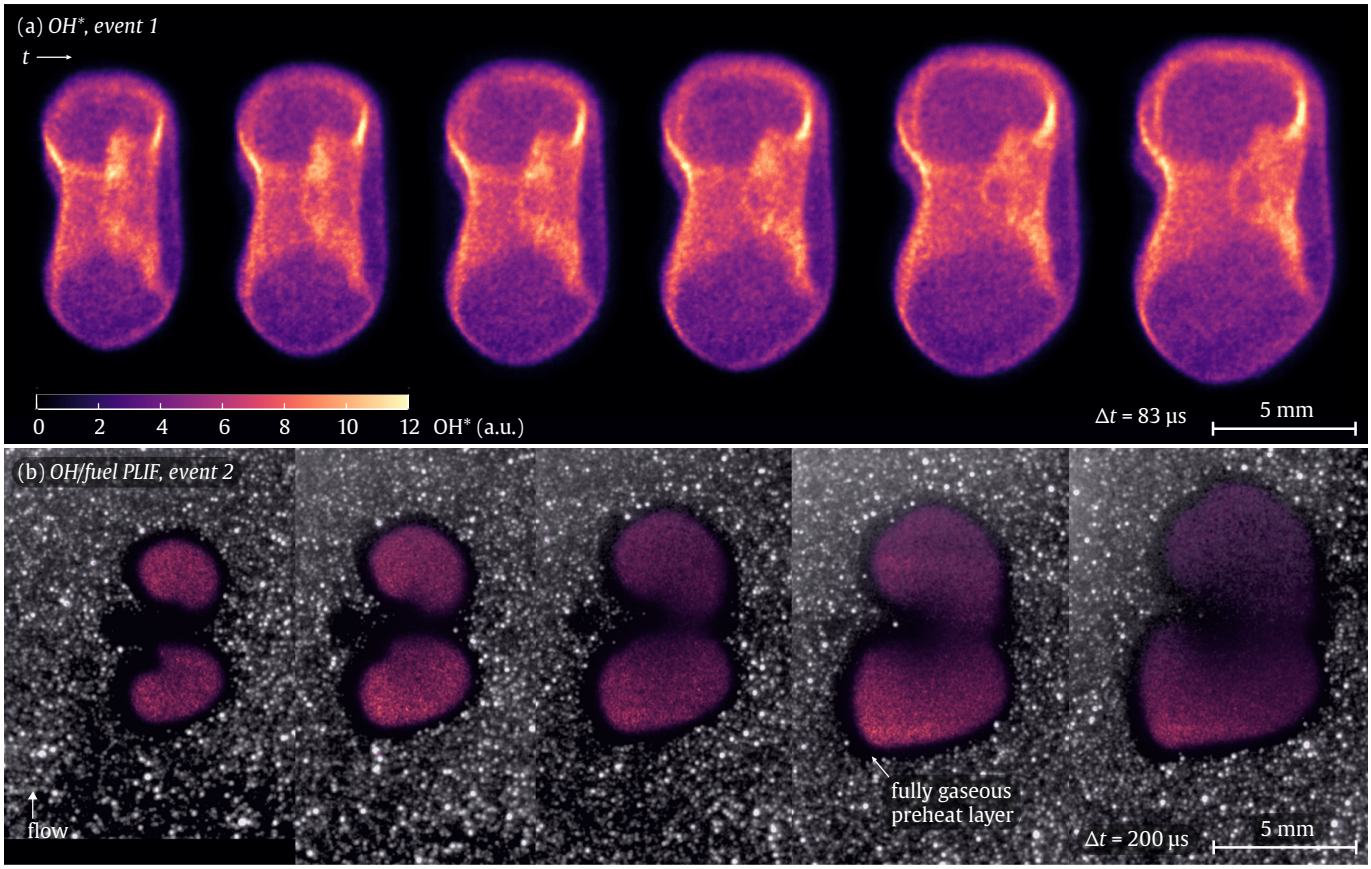

Figure 14: Example of independent events visualised by (a) OH* and (b) OH/fuel PLIF – ATJ-8, ϕ=1.4, d_{32}=16 µm.

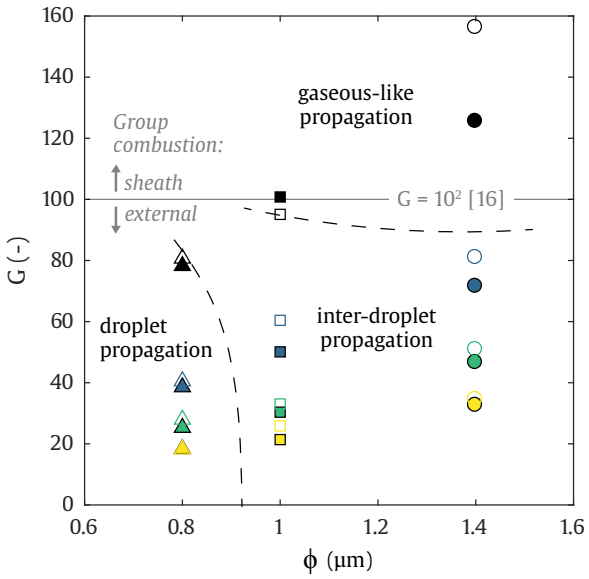

Figure 15: Ignition-mode diagram for the present experimental conditions. Symbols and colours are the same used in Fig. 7.

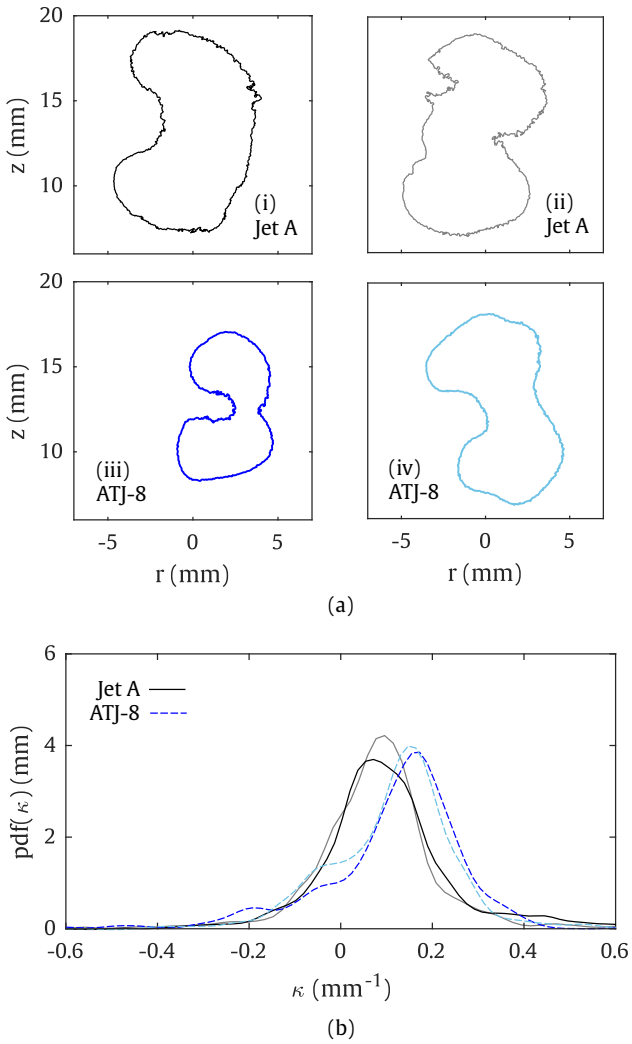

Figure 16: Shape of flame kernels (a) and respective curvature pdfs (b) for Jet A and ATJ-8 at 1.35 ms after the spark – ϕ=1.4, d_{32}=16 µm.